Received: 9 August 2019 | Revised: 12 November 2019 | Accepted: 10 January 2020

DOI: 10.1002/aic.16920

PARTICLE TECHNOLOGY AND FLUIDIZATION

AIChE JOURNAL

Estimation of the dominant size enlargement mechanism in spray fluidized bed processes

Christian Rieck[1] | Andreas Bück[2] | Evangelos Tsotsas[1]

[1]Thermal Process Engineering, Otto von Guericke University, Magdeburg, Germany

[2]Institute of Particle Technology, FAU Erlangen-Nuremberg, Erlangen, Germany

Correspondence
Christian Rieck, Thermal Process Engineering, Otto von Guericke University, Universitätsplatz 2, Magdeburg 39106, Germany.
Email: christian.rieck@ovgu.de

Funding information
DFG, Grant/Award Number: 61375930—SFB/CRC 814; Deutsche Forschungsgemeinschaft, Grant/Award Number: A2-SPP 1679

Abstract

This work deals with estimating the dominant size enlargement mechanism in spray fluidized beds. A new process model is presented, which consists of population balances and a heat- and mass-transfer model. New methods to incorporate the wet surface fraction and the Stokes criterion are proposed, which allow for the probability of wet collisions and the probability of successful wet collisions to be calculated. The product of these parameters, the probability of successful collisions, is linked to the dominant size enlargement mechanism. Simulation studies were performed to investigate the influence of inlet gas temperature, viscosity, droplet size, and contact angle on the probability of successful collisions. Further simulation results based on experiments available in literature suggest that exceeding a probability of successful collisions of 0.001 is sufficient for agglomeration to become dominant. Otherwise, layering will be the dominant size enlargement mechanism. Finally, regime maps of layering and agglomeration are constructed.

KEYWORDS

agglomeration, layering, size enlargement mechanism, spray fluidized bed

1 | INTRODUCTION

Spray fluidized beds are often used for particle formulation processes in the pharmaceutical, agricultural, and food industries to produce particulate products from solid containing liquids.[1] In a spray fluidized bed, the liquid is sprayed on a particle bed fluidized by a hot gas stream inducing size enlargement of the particles. Depending on the process conditions and material properties, size enlargement by agglomeration or layering may occur, see Figure 1. Agglomeration denotes the formation of particles consisting of several primary particles connected by binding forces, which are mainly caused by material bridges (i.e., liquid or solid binder bridges) in the considered processes. Interparticle collisions at wet spots created by repeated droplet deposition and subsequent drying of liquid bridges lead to the formation of agglomerates. Agglomerated particles are produced for applications such as enhancing re-dispersion behavior of food powders[2,3] and improving compactibility and dosing accuracy prior to tabletting of pharmaceutical powders.[3,4] In layering, interparticle collisions do not contribute to particle growth. Instead, the particles grow by repeated droplet deposition, drying, and solidification of the liquid droplets, leading to a solid layer around the initial particles. In coating processes (core particle material and sprayed solid material are different), the solid layer may be used for sustained release, taste and odor masking, and to protect the core particle from environmental influences.[1-6] In layering granulation (core particle material and sprayed solid material are identical), the main objective is to transform the liquid material into a particulate product with a specified size distribution[7] (e.g., when producing fertilizers[8]). Generally, both size enlargement mechanisms may occur simultaneously, but depending on the application of the product, only one size enlargement mechanism should be dominant.

The border between agglomeration and layering has been investigated experimentally in studies dealing with layering processes, in which agglomeration is an undesired side effect. Dewettinck et al[9,10] focused on the detection of defluidization caused by rapid agglomeration in coating processes. Moraga et al,[8] Hemati et al,[11] and Hede et al[12,13] deal with the direct measurement of the mass fraction of agglomerated particles in coating and layering granulation processes. These studies indicate that agglomeration is more pronounced if the

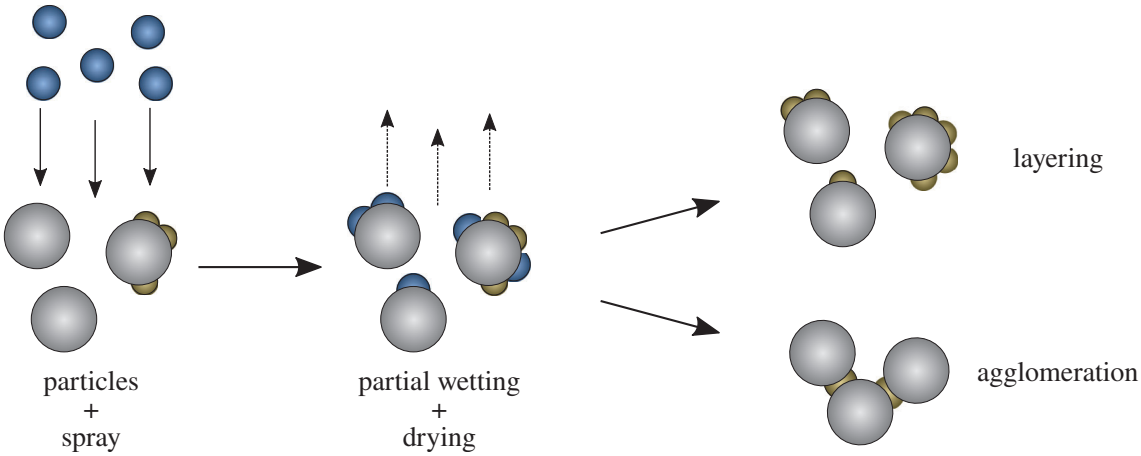

FIGURE 1 Scheme of the two size enlargement mechanisms in spray fluidized bed processes [Color figure can be viewed at wileyonlinelibrary.com]

particle size, the temperature in the bed, the mass flow rate, and the evaporation capacity of the fluidization gas are decreased, and the spraying rate and the droplet size are increased. Theoretical investigations of the border between agglomeration and layering are also available in the literature. Boerefijn and Hounslow[14] and Boerefijn et al[15] suggest a classification of the dominant size enlargement mechanism using a dimensionless number called Flux-number based on the works of Akkermans et al[16] and Wasserman et al.[17] This parameter takes the particle density, the excess gas velocity of the fluidization gas, and the mass flux of the spray (related to the bed surface area wetted by the spray cone of the nozzle) into account, but does not consider the temperature or the drying capacity of the fluidization gas, which have been identified to influence the dominant size enlargement mechanism. Another classification is given by Ennis et al[18] based on the works of Davis[19] and Barnocky and Davis.[20] This approach deals with predicting the outcome of a binary, normal collision (agglomeration or rebound) between particles on the single particle level. Two dimensionless numbers, the viscous and critical Stokes number, are used in this criterion taking into account microlevel parameters such as liquid film height and viscosity, particle size, and particle restitution coefficient. Donahue et al[21,22] present theoretical and experimental work on the outcome of oblique collisions between particles. They have found that particles may separate after successful agglomeration, although the Stokes criterion (derived for normal collisions) is met. This observation is attributed to centrifugal forces arising from the rotational motion of the agglomerate, leading to breakage of the liquid bridge. A dimensionless number (i.e., the centrifugal number) is proposed to characterize the influence of centrifugal forces. According to Donahue et al,[21] both the Stokes criterion and the centrifugal number should be used to predict whether collisions lead to agglomeration. Hede et al[13] and Villa et al[23] tested both the Flux-number and the Stokes criterion (for normal collisions) experimentally. Though both criteria predicted layering to be the dominant size enlargement mechanism, agglomeration has also been observed indicating that more complex criteria are required.

Modeling the kinetics of both size enlargement mechanisms is of great interest in the literature, see Heinrich and Mörl,[24] Vreman et al,[25] Silva et al,[26] Rieck et al[27] for layering and Hounslow et al,[28] Kumar et al,[29] Hussain et al[30] for agglomeration. In case of layering, the kinetics can be calculated directly from the process parameters and particle properties, while in case of agglomeration the situation is more complex. Usually, the kinetics of agglomeration is described by an aggregation kernel, which depends on time and particle size. Several kernel equations, mechanistic or empirical, have been proposed in literature.[31] Selecting one of them can be done by trial and error or by fitting free parameters in empirical kernels. Hussain et al[30] present a study on modeling the aggregation kernel as a result of process conditions and material properties, which is achieved by incorporating the probability of wet collisions and the probability of successful wet collisions in the aggregation kernel. They show that these parameters are related to the wet surface fraction and the Stokes criterion, respectively. By extending a one-dimensional population balance model to capture additional properties such as the number of wet particles and droplets, the wet surface fraction was calculated and the probability of successful wet collisions was estimated based on the Stokes criterion using the mean particle diameter. The wet surface fraction has been used in modeling spray fluidized bed processes by Heinrich and Mörl.[24] However, they assume that the sprayed liquid forms a coherent film with an arbitrary height on the particle surface and this model has not been used to estimate the dominant size enlargement mechanism.

In this study, a model to estimate the dominant size enlargement mechanism for spray fluidized bed layering processes is presented. Based on the work of Hussain et al,[30] the probability of wet collisions and the probability of successful wet collisions are modeled. In order to calculate the probability of wet collisions, a new model for the wet surface fraction including the geometry of deposited droplets is presented. Additionally, a new model for calculating the probability of successful wet collisions using the complete particle-size distribution is derived. From these parameters, the probability of successful collisions is calculated, which is used to estimate if either layering or

agglomeration will be dominant. A simulation study is used to investigate the influence of temperature, viscosity, and wetting parameters (droplet size and contact angle) on the dominant size enlargement mechanism. Based on experimental data and simulation results, a classification of the size enlargement mechanism based on the probability of successful collisions is proposed, which can be used to create regime maps.

2 | MODELING

2.1 | Estimating the probability of successful collisions

The modeling approach by Hussain et al[30] shows that the aggregation kernel depends on the probability of a wet collision (at least one droplet must be involved in a collision for agglomeration to happen) and on the probability of a successful wet collision (probability that the kinetic energy is dissipated in a wet collision, leading to agglomeration). The product of these parameters, which is the probability of successful collisions $P_{\mathrm{coll,suc}}$, may then be used to estimate the dominant size enlargement mechanism:

$$P_{\mathrm{coll,suc}} = P_{\mathrm{coll,wet}} \cdot P_{\mathrm{coll,wet,suc}}. \tag{1}$$

The dominant mechanism will be layering if $P_{\mathrm{coll,\ suc}} \to 0$. This may be due to a low probability of wet collisions ($P_{\mathrm{coll,\ wet}} \to 0$), a low probability of successful wet collisions ($P_{\mathrm{coll,\ wet,\ suc}} \to 0$), or both. If $P_{\mathrm{coll,suc}}$ is sufficiently large (ideally if $P_{\mathrm{coll,\ suc}} \to 1$), agglomeration will be the dominant mechanism. This condition will certainly be fulfilled if both the probability of wet collisions and the probability of successful wet collisions approach unity ($P_{\mathrm{coll,\ wet}} \to 1$ and $P_{\mathrm{coll,\ wet,\ suc}} \to 1$). Note that in Equation (1) the influence of breakage of either liquid or dry bridges is not included. At this stage it is assumed that breakage does not dominate the process and therefore the probability of successful collisions can be used as a suitable parameter to estimate the dominant size enlargement mechanism. In the following sections, modeling of the considered probabilities is presented.

2.1.1 | Probability of wet collisions

In this approach, following Rajniak et al,[32] a simplified situation is considered, assuming that all particles are wet and have the same wet surface fraction Ψ. Since only binary collisions are taken into account, at least one droplet, but not more than two droplets can be involved in a wet collision. The probability of wet collisions is then equal to the probability that at least one droplet is involved in a collision. This parameter can be calculated from the probabilities of the individual events (exactly one droplet and exactly two droplets take part in a collision):

$$P_{\mathrm{coll,wet}} = 2\Psi(1-\Psi) + \Psi^2 = 2\Psi - \Psi^2. \tag{2}$$

2.1.2 | Probability of successful wet collisions

The probability of successful wet collisions is calculated based on the Stokes criterion. In this approach, we consider normal collisions as well as spherical, nondeformable particles, which are always larger (in diameter) than the sprayed droplets. The criterion uses a viscous and a critical Stokes number to determine the outcome of a binary collision between spherical particles of equal size, which is either rebound, or agglomeration, see Ennis et al[18] and Barnocky and Davis[20]:

$$\mathrm{St} = \frac{4}{9}\frac{\varrho_{\mathrm{p}} x v_{\mathrm{coll}}}{\eta} \text{ and } \mathrm{St}_{\mathrm{crit}} = \left(1+\frac{1}{e}\right)\ln\left(\frac{h}{h_{\mathrm{a}}}\right). \tag{3}$$

In this equation, x is the particle diameter, ϱ_{p} is the particle density, v_{coll} is the collision velocity, η is the viscosity of the liquid, e is the restitution coefficient of the particles, and h and h_{a} represent the height of the liquid layer and the surface asperities of the particle material, respectively. A binary collision results in agglomeration if the critical Stokes number exceeds the viscous Stokes number. Otherwise, the collision results in rebound of the colliding particles:

$$\text{Outcome} = \begin{cases} \text{Agglomeration} & \mathrm{St} \le \mathrm{St}_{\mathrm{crit}} \\ \text{Rebound} & \text{Otherwise.} \end{cases} \tag{4}$$

Rearranging, a critical diameter x_{crit} can be calculated:

$$x_{\mathrm{crit}} = \frac{9}{4}\frac{\eta}{\varrho_{\mathrm{p}} v_{\mathrm{coll}}}\left(1+\frac{1}{e}\right)\ln\left(\frac{h}{h_{\mathrm{a}}}\right). \tag{5}$$

Particles with a diameter smaller than or equal to this value have the possibility to agglomerate upon a wet collision since the Stokes criterion is fulfilled. The fraction of particles f_{agg} below this value can be obtained from the normalized number-based particle-size distribution q_0:

$$f_{\mathrm{agg}} = \int_0^{x_{\mathrm{crit}}} q_0 \, \mathrm{d}x. \tag{6}$$

Figure 2 shows a normalized particle-size distribution q_0 (normal distribution with a mean diameter of 0.2 mm and a standard deviation of 0.05 mm). In this example, the critical diameter is equal to 0.15 mm and f_{agg} equals 0.16.

Since the Stokes criterion presented by Ennis et al[18] is developed for spherical particles of equal size, the diameter of both colliding particles should be smaller than x_{crit} for agglomeration to occur. As shown by several authors[33-35] the Stokes criterion can be generalized to account for the collision of unequal spheres by using the harmonic mean particle size. As a result, a wet collision leads to agglomeration if the harmonic mean of the diameters of the colliding particles is smaller than or equal to the critical diameter:

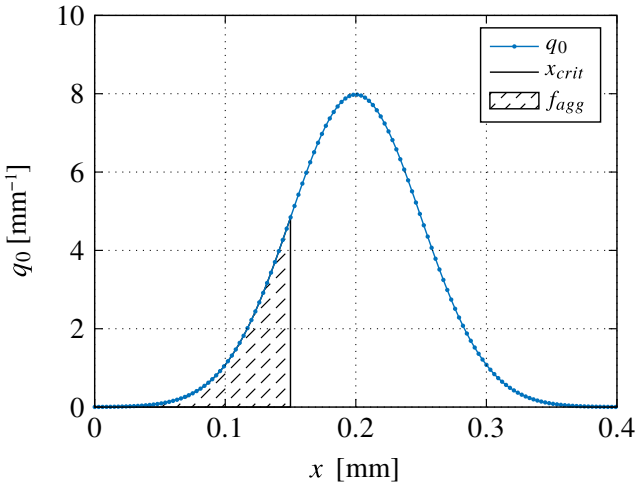

FIGURE 2 Plot of a particle-size distribution (mean value and *SD* equal to 0.2 and 0.05 mm, respectively) with a critical diameter equal to 0.15 mm and the corresponding fraction of particles with fulfilled Stokes criterion [Color figure can be viewed at wileyonlinelibrary.com]

$$\frac{2x_1x_2}{x_1+x_2} \le x_{\text{crit}}. \tag{7}$$

In this case, the situation is more complex since one of the two diameters may be larger than x_{crit} as long as the harmonic mean is still smaller than x_{crit}. Rearranging yields x_2 as a function of x_1. Since a pole exists at $x_{crit}/2$, two cases are obtained:

$$x_2 \ge \frac{x_1x_{\text{crit}}}{2x_1-x_{\text{crit}}} \quad \text{for} \quad x_1 < \frac{x_{\text{crit}}}{2}, \tag{8}$$

$$x_2 \le \frac{x_1x_{\text{crit}}}{2x_1-x_{\text{crit}}} \quad \text{for} \quad x_1 > \frac{x_{\text{crit}}}{2}. \tag{9}$$

Evaluating the equations shown above for the limit cases yields:

$$0 < x_1 < \frac{x_{\text{crit}}}{2}: \quad \lim_{x_1\to 0^+} \frac{x_1x_{\text{crit}}}{2x_1-x_{\text{crit}}} = 0 \quad \text{and} \quad \lim_{x_1\to \frac{x_{\text{crit}}}{2}^-} \frac{x_1x_{\text{crit}}}{2x_1-x_{\text{crit}}} = -\infty, \tag{10}$$

$$\frac{x_{\text{crit}}}{2} < x_1 < \infty: \quad \lim_{x_1\to \frac{x_{\text{crit}}}{2}^+} \frac{x_1x_{\text{crit}}}{2x_1-x_{\text{crit}}} = \infty \quad \text{and} \quad \lim_{x_1\to \infty} \frac{x_1x_{\text{crit}}}{2x_1-x_{\text{crit}}} = \frac{x_{\text{crit}}}{2}. \tag{11}$$

Both cases are shown in Figure 3a for the same example as in Figure 2. For $x_1 < x_{crit}/2$, x_2 must be larger than the value calculated with Equation (8). This value starts at zero and decreases asymptotically to $-\infty$ as $x_1 \to x_{crit}/2$. Since in the considered process only positive values for x_2 are reasonable, this variable can attain any value while $x_1 < x_{crit}/2$ in order to fulfill the condition given in Equation (7), leading to agglomeration. For $x_1 > x_{crit}/2$, x_2 must be smaller than the value calculated with Equation (9). The value starts at ∞ and decreases asymptotically to $x_{crit}/2$. Here, the particle-size distribution plays a role in whether the condition in Equation (7) is fulfilled and agglomeration occurs.

The fraction of particles with a fulfilled Stokes criterion can be calculated similar to Equation (6). However, in this case, its value depends on x_1. From the above shown analysis it can be deduced that for $x_1 < x_{crit}/2$, the corresponding value of f_{agg} is unity since x_2 can take any value. For $x_1 > x_{crit}/2$, f_{agg} can be calculated as shown above, leading to:

$$f_{\text{agg}}(x_1) = \begin{cases} 1 & x_1 < \frac{x_{\text{crit}}}{2} \\ \int_0^{x_2} q_0 \mathrm{d}x & x_1 > \frac{x_{\text{crit}}}{2}. \end{cases} \tag{12}$$

Figure 3b shows f_{agg} as a function of x_1 for the current example.

The probability of successful wet collisions can then be calculated from f_{agg} depending on x_1 and the probability distribution of the particle size, which is given by the normalized particle-size distribution q_0:

$$P_{\text{coll, wet, suc}}(x, x_1) = \int_0^{\infty} f_{\text{agg}}(x_1) q_0(x) \mathrm{d}x. \tag{13}$$

2.1.3 | Verification of the probability of successful wet collisions

In order to verify the proposed model used to calculate the probability of successful wet collisions, it is compared to results obtained with a Monte Carlo model. In the Monte Carlo model, a set of particles with different diameters is created according to a given particle-size distribution. In this example, the same distribution as the one shown in Figure 2 is used to create a set of 10^8 particles. Then, binary collisions between the particles are mimicked by randomly choosing two collision partners from the particle set. In each collision, the diameters of the collision partners are checked. A collision is then labeled "successful" if the harmonic mean diameter is smaller than a given critical value x_{crit}. After a certain number of collisions, which is in this case 10^7, the fraction of successful wet collisions is calculated. Note that other than checking if a collision is successful, nothing else happens in the Monte Carlo model (i.e., agglomeration of the collision partners) since the only purpose is verifying Equation (13). The Monte Carlo simulation was then performed for different values of x_{crit} and for each case, the result is compared to Equation (13) (see Section 3).

In order to calculate the probability of successful collisions, which is used to estimate the dominant size enlargement mechanism, a process model is required to provide the necessary parameters. The probability of wet collisions (see Equation 2) requires the wet surface fraction, which is calculated as a part of a novel spray fluidized bed drying model. Looking at the processes from the point of view of layering, a population balance model for layering growth is used to calculate the transient behavior of the particle-size distribution, which is required to calculate the probability of successful wet collisions (see Equation 13). In the following sections, the drying models used here are presented.

2.2 | Drying model

2.2.1 | Wet surface fraction

The wet surface fraction Ψ is defined as the ratio between the wet surface area A_{pl} (interface between particle and liquid phase) and the total particle surface area A_p. Changes in the wet surface area can be attributed to changing wet surface fraction due to drying and changing total particle surface area due to size enlargement:

$$\frac{dA_{pl}}{dt} = \frac{d}{dt}(\Psi A_p) = \Psi \frac{dA_p}{dt} + A_p \frac{d\Psi}{dt}. \tag{14}$$

The change of total surface area depends on the transient behavior of the second moment of the particle-size distribution n:

$$\Psi \frac{dA_p}{dt} = \Psi \pi \int_0^\infty x^2 \frac{\partial n}{\partial t} dx. \tag{15}$$

In contrast to Heinrich and Mörl,[24] who assume a coherent film, the liquid phase is here described by a number of individual droplets deposited on the particle surface. The droplets are assumed to be monodisperse, each covering a certain surface area of the particle. Coalescence or overlapping of droplets is not considered. Using these assumptions, the change in wet surface area depends on the area covered by a single droplet $A_{contact}$ (footprint of the droplet), the mass of the droplet M_{drop} and the mass of the liquid phase M_l:

$$\frac{dA_{pl}}{dt} = \frac{A_{contact}}{M_{drop}} \frac{dM_l}{dt}. \tag{16}$$

Combining Equation (14) to Equation (16) yields the time derivative of the wet surface fraction, assuming that it does not exceed unity:

$$\frac{d\Psi}{dt} = \begin{cases} \frac{1}{A_p}\left[\frac{A_{contact}}{M_{drop}}\frac{dM_l}{dt} - \Psi\pi\int_0^\infty x^2\frac{\partial n}{\partial t}dx\right] & \Psi < 1 \\ 0 & \text{Otherwise.} \end{cases} \tag{17}$$

The droplet geometry is described by equations proposed by Meric and Erbil,[36] assuming that droplets take the form of a spherical cap as indicated in Figure 4. The contact area $A_{contact}$, the curved surface area of a droplet A_{drop}, and the droplet height h_{drop} can be calculated from the droplet volume V_{drop} and the contact angle θ:

$$A_{contact} = \frac{\pi}{4} x_{contact}^2 \quad \text{with} \quad x_{contact} = 2\left(\frac{3V_{drop}}{\pi}\frac{\sin^3\theta}{2-3\cos\theta+\cos^3\theta}\right)^{1/3}, \tag{18}$$

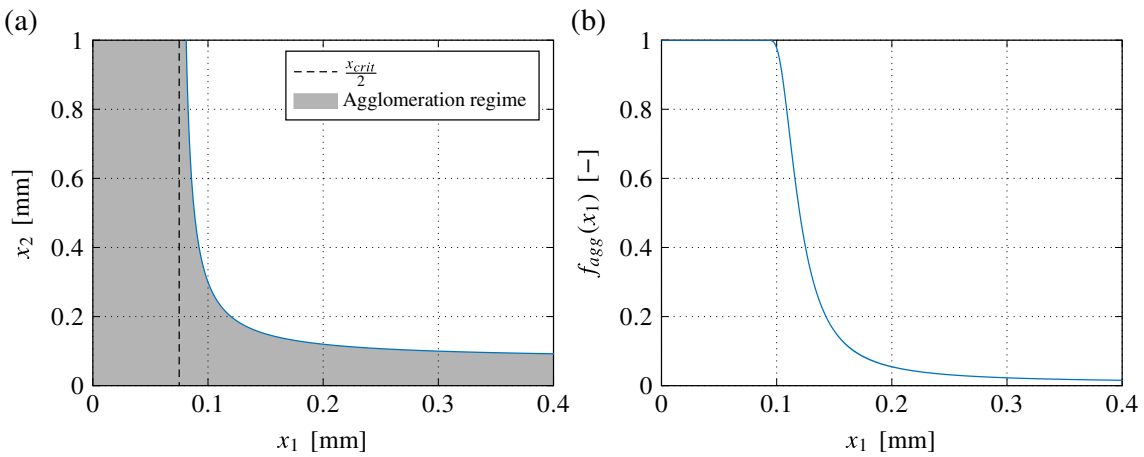

FIGURE 3 Plot of the particle size x_2 (a) and the corresponding fraction of particles with fulfilled Stokes criterion f_{agg} (b) as a function of x_1 for the same particle-size distribution and critical diameter as in Figure 2 [Color figure can be viewed at wileyonlinelibrary.com]

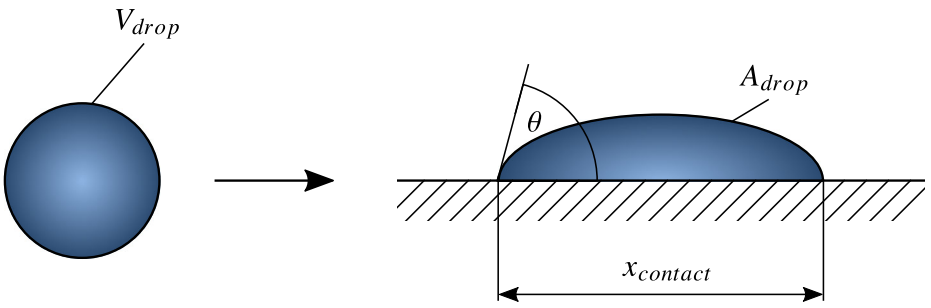

FIGURE 4 Illustration of a droplet before (sphere) and after deposition (spherical cap) on a flat surface [Color figure can be viewed at wileyonlinelibrary.com]

$$A_{\text{drop}} = \frac{1}{2}\frac{\pi x_{\text{contact}}^2}{1+\cos\theta}, \tag{19}$$

$$h_{\text{drop}} = \left(\frac{V_{\text{drop}}}{\pi}\left(\frac{1}{1-\cos\theta}-\frac{1}{3}\right)^{-1}\right)^{1/3}. \tag{20}$$

In this way, the influence of droplet size (volume) and contact angle on both the probability of wet collisions (contact area) and the probability of successful wet collisions (droplet height) can be taken into account. Note that the above shown droplet properties are calculated using the initial droplet volume. In this study, shrinkage and an increasing viscosity of deposited droplets during drying is therefore not included. Extensions in this direction can be made without conceptional difficulties.

2.2.2 | Heat and mass transfer

Modeling of heat and mass transfer in fluidized beds has been investigated in the literature, see Burgschweiger et al[37] for fluidized bed drying and Heinrich and Mörl[24] for spray fluidized bed layering. Both models are very accurate, but complex.

The heat- and mass-transfer model for spray fluidized beds presented in this study relies on several assumptions for simplification. Three phases are considered (liquid film, particle, and gas phase) and the main assumptions are:

- no distinction between suspension and bubble phase,
- perfectly mixed solid and liquid film phase, and
- plug flow of the gas phase.

The heat and mass flow rates considered in the model are shown in Figure 5: heat can be exchanged between the gas and particle phase (index "gp"), between the particle and liquid phase (index "pl"), and between the gas and liquid phase (index "gl"). Mass and enthalpy transfer between the liquid and the gas due to evaporation is taken into account. As a result of the main model assumptions, the particle and liquid film phase do not depend on the spatial position in the fluidized bed. Since the gas phase is modeled assuming plug flow, the mass and enthalpy of the gas phase depend on the spatial position in the fluidized bed, which is represented by a normalized height coordinate ζ. In the following, the resulting mass and enthalpy balances are presented.

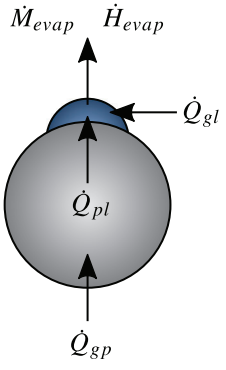

FIGURE 5 Scheme of the considered mass, enthalpy, and heat flow rates in the presented model [Color figure can be viewed at wileyonlinelibrary.com]

Mass and enthalpy balances

The mass of water in the gas phase $M_{\text{w,g}}$ is transported along the spatial coordinate ζ with a rate equal to $\dot{M}_{\text{w,g}}$ and changes due to the mass flow rate of evaporation $\dot{M}_{\text{evap}}$. The enthalpy of the gas phase H_{g} is transported along ζ as well and changes due to the enthalpy flow rate of evaporation $\dot{H}_{\text{evap}}$, and the heat flow rates between the gas and particle $\dot{Q}_{\text{gp}}$ and gas and liquid phase $\dot{Q}_{\text{gl}}$:

$$\frac{\partial M_{\text{w,g}}}{\partial t} = -\frac{\partial \dot{M}_{\text{w,g}}}{\partial \zeta} + \dot{M}_{\text{evap}}, \tag{21}$$

$$\frac{\partial H_{\text{g}}}{\partial t} = -\frac{\partial \dot{H}_{\text{g}}}{\partial \zeta} + \dot{H}_{\text{evap}} - \dot{Q}_{\text{gp}} - \dot{Q}_{\text{gl}}. \tag{22}$$

The mass of the liquid film phase M_{l} depends on the mass flow rate of the sprayed liquid $\dot{M}_{\text{spray,l}}$ and the mass flow rate of evaporation. The liquid film enthalpy H_{l} changes due to evaporation and the heat transfer between the gas and liquid $\dot{Q}_{\text{gl}}$ and the particle and liquid phase $\dot{Q}_{\text{pl}}$, respectively:

$$\frac{\mathrm{d}M_{\text{l}}}{\mathrm{d}t} = \dot{M}_{\text{spray, l}} - \bar{\dot{M}}_{\text{evap}}, \tag{23}$$

$$\frac{\mathrm{d}H_{\text{l}}}{\mathrm{d}t} = -\bar{\dot{H}}_{\text{evap}} + \bar{\dot{Q}}_{\text{gl}} + \dot{Q}_{\text{pl}}. \tag{24}$$

The mass of the particle phase M_{p} is calculated from the third moment of the particle-size distribution. The enthalpy of the particle phase H_{p} depends on the heat flow rates between the particle and the gas phase $\dot{Q}_{\text{gp}}$ and between the particle and the liquid phase $\dot{Q}_{\text{pl}}$:

$$M_{\text{p}} = \frac{\pi}{6}\varrho_{\text{p}}\mu_3 = \frac{\pi}{6}\varrho_{\text{p}}\int_0^\infty x^3 n \mathrm{d}x, \tag{25}$$

$$\frac{\mathrm{d}H_{\text{p}}}{\mathrm{d}t} = \bar{\dot{Q}}_{\text{gp}} - \dot{Q}_{\text{pl}}. \tag{26}$$

Since the mass flow rate of evaporation, the corresponding enthalpy flow rate and the heat flow rates between the gas phase and the liquid phase, and between the gas phase and the particle phase depend on the spatial location ζ, their average values are used in the above shown mass and enthalpy balances for the film and particle phase. The averaged values are calculated as follows:

$$\bar{\dot{M}}_{\text{evap}} = \int \dot{M}_{\text{evap}} \mathrm{d}\zeta, \tag{27}$$

$$\bar{\dot{H}}_{\text{evap}} = \int \dot{H}_{\text{evap}} \mathrm{d}\zeta, \tag{28}$$

$$\bar{\dot{Q}}_{\text{gl}} = \int \dot{Q}_{\text{gl}} \mathrm{d}\zeta, \tag{29}$$

$$\bar{\dot{Q}}_{\text{gp}} = \int \dot{Q}_{\text{gp}} \mathrm{d}\zeta. \tag{30}$$

Kinetics

The evaporation rate is calculated using the following equation:

$$\dot{M}_{\text{evap}} = \beta \varrho_{\text{g}} A_{\text{gl}} \left(Y^{*}(T_{\text{l}}) - Y\right) \quad \text{with} \quad A_{\text{gl}} = \Psi A_{\text{p}} \frac{A_{\text{drop}}}{A_{\text{contact}}}. \tag{31}$$

In this equation, β is the mass-transfer coefficient, ϱ_g is the density of the gas, A_{gl} is the area of the gas–liquid interface (curved surface area of the droplets), $Y^*(T_{\text{l}})$ is the saturation moisture content of the gas at liquid film temperature T_{l} calculated according to Glück,[38] and Y is the moisture content of the bulk gas. Note that the wet surface fraction directly influences the evaporation mass flow rate since it is part of A_{gl}, which depends on the wet surface fraction, the total surface area of the particles, and the ratio between the curved surface area and the footprint of deposited droplets. If $\Psi \to 1$ the evaporation rate reaches its maximum and if $\Psi \to 0$ the evaporation rate goes to zero, resembling the behavior of particles which first dry from their surface and then from their interior, as shown by Burgschweiger et al.[37]

The mass-transfer coefficient β is obtained from the Sherwood number Sh:

$$\beta = \frac{\mathrm{Sh}\delta}{x}, \mathrm{Sh} = f(\mathrm{Re},\ \mathrm{Sc}), \tag{32}$$

which is calculated here based on empirical correlations given by Groenewold and Tsotsas.[39] The Sherwood number depends on the Reynolds number Re and the Schmidt number Sc. The mass-transfer coefficient then follows from the Sherwood number Sh, the diffusion coefficient of water vapor in the gas δ, and the particle diameter x.

The moisture content of the bulk gas Y is calculated from the mass of water in the gas phase and the mass of dry air in the fluidized bed, see Equation (33). In this equation, ε_{bed}, x_{bed}, and h_{bed} are the porosity, diameter, and the height of the fluidized bed, respectively. The bed porosity is calculated according to correlations given by Martin[40] and the bed height follows from the bed mass and volume (cylindrical fluidized bed chamber). In a similar way, the moisture content of the particles X can be calculated using the liquid film mass and the mass of the particles, see Equation (34):

$$Y = \frac{M_{\text{w,g}}}{M_{\text{g,dry}}} \quad \text{with} \quad M_{\text{g,dry}} = \varepsilon_{\text{bed}} \frac{\pi}{4} x_{\text{bed}}^2 \varrho_{\text{g}} h_{\text{bed}}, \tag{33}$$

$$X = \frac{M_{\text{l}}}{M_{\text{p}}}. \tag{34}$$

The enthalpy and heat flow rates used in the differential equations shown above are calculated as follows:

$$\dot{H}_{\text{evap}} = \dot{M}_{\text{evap}} (c_{\text{v}} T_{\text{l}} + \Delta h_{\text{evap}}), \tag{35}$$

$$\dot{Q}_{\text{gl}} = \alpha_{\text{gl}} A_{\text{gl}} (T_{\text{g}} - T_{\text{l}}), \tag{36}$$

$$\dot{Q}_{\text{pl}} = \alpha_{\text{pl}} A_{\text{pl}} (T_{\text{p}} - T_{\text{l}}) \quad \text{with} \quad A_{\text{pl}} = \Psi A_{\text{p}}, \tag{37}$$

$$\dot{Q}_{\text{gp}} = \alpha_{\text{gp}} A_{\text{gp}} (T_{\text{g}} - T_{\text{p}}) \quad \text{with} \quad A_{\text{gp}} = (1 - \Psi) A_{\text{p}}. \tag{38}$$

In these equations, α is the heat-transfer coefficient between the respective phases. The gas-particle heat-transfer coefficient α_{gp} follows from the corresponding Nusselt number Nu_{gp}, the particle diameter x, and the thermal conductivity λ_{g} of the gas:

$$\alpha_{\text{gp}} = \frac{\mathrm{Nu}_{\text{gp}} \lambda_{\text{g}}}{x}, \quad \mathrm{Nu}_{\text{gp}} = \mathrm{Sh}\,\mathrm{Le}^{-1/3}. \tag{39}$$

The Nusselt number is calculated from the Sherwood number and the Lewis number Le. The gas–liquid heat-transfer coefficient α_{gl} is assumed to be equal to α_{gp}, as in Heinrich and Mörl.[24] The heat transfer between the particle and the droplet is assumed to be purely conductive, neglecting any convection. For this case (contact between a fluid and a sphere), α_{pl} can be calculated with a Nusselt number equal to two. The particle–liquid interface A_{pl} in Equation (37) is the wet surface area and the gas–particle interface A_{gp} in Equation (38) is the dry surface area of the particles.

The following equations are used to relate the temperature of each phase with the corresponding enthalpy:

$$H_{\text{g}} = M_{\text{g,dry}} (c_{\text{g}} T_{\text{g}} + Y (c_{\text{v}} T_{\text{g}} + \Delta h_{\text{evap}})), \tag{40}$$

$$H_{\text{p}} = M_{\text{p}} c_{\text{p}} T_{\text{p}}, \tag{41}$$

$$H_{\text{l}} = M_{\text{l}} c_{\text{l}} T_{\text{l}}. \tag{42}$$

In these equations, c_{g}, c_{v}, c_{p}, and c_{l} denote the specific heat capacities of the gas phase, vapor, the particle, and the liquid phase.

2.3 | Population balance model

In the literature, several approaches exist to model particle growth due to layering in spray fluidized bed processes. Compartment models divide the process chamber into two or more coupled zones (i.e., a spray zone and a drying zone) to account for dispersion of the particle-size distribution during the growth process, see Sherony,[41] Wnukowski and Setterwall,[42] Maronga and Wnukowski,[43] and Rieck et al.[27] As shown by Neugebauer et al,[44] layering growth can also be modeled using a single compartment approach, which is used in this study for simplification. The resulting growth model is a single one-

dimensional population balance equation describing the transient behavior of the particle-size distribution n due to layering:

$$\frac{\partial n}{\partial t} = -\frac{\partial Gn}{\partial x}. \tag{43}$$

The growth rate G is calculated according to Rieck et al,[27] assuming that the distribution of the sprayed material is related to an arbitrary moment μ_j of the particle-size distribution. Depending on the type of the moment (index j), the growth rate G_j can be calculated directly from process and material parameters:

$$G_j = \frac{2\dot{M}_{spray,s}}{\varrho_s \pi (1-\varepsilon)} \frac{x^{j-2}}{\mu_j} \quad \text{with} \quad \mu_j = \int_0^\infty x^j n dx \tag{44}$$

In this equation, $\dot{M}_{spray,s}$ is the mass flow rate of the sprayed solid material, ϱ_s is the density of the sprayed solid material (without pores), and ε is the porosity of the solid layer. The total growth rate G can then be calculated as a linear combination of G_k using the constants λ_k:

$$G = \sum_k \lambda_k G_k \quad \text{with} \quad \sum_k \lambda_k = 1 \tag{45}$$

In this work, $\lambda_2 = 1$, which leads to $G = G_2$. As a result, the distribution of the sprayed material is related to the particle surface area following the idea proposed by Mörl et al.[45] In all simulations presented in this study, the porosity of the solid layer is set to 30%.

Layering growth leads to a changing particle density, which can be taken into account by calculating a mean particle density ϱ_p based on the third moment of the particle-size distribution:

$$\varrho_p = \varrho_{p,0} \frac{\mu_{3,0}}{\mu_3} + \varrho_s (1-\varepsilon) \frac{\mu_3 - \mu_{3,0}}{\mu_3}. \tag{46}$$

In this equation, $\varrho_{p,0}$ is the initial particle density, μ_3 represents the third moment of the particle-size distribution and $\mu_{3,0}$ is the initial value of the third moment.

2.4 | Solution of the model equations

The system of differential equations is solved numerically using the solver ode15s provided by MATLAB. The partial differential equations given in Equations (21), (22), and (43), are discretized using a finite volume scheme. Additionally, in the case of Equation (43), a flux-limiter function given by Koren[46] is used to reduce numerical diffusion.

2.4.1 | Simulation study

A simulation study was performed to investigate the influence of inlet gas temperature, viscosity, and wetting parameters (droplet size and contact angle) on the dominant size enlargement mechanism represented by the probability of successful collisions.

The simulation parameters and the used initial and boundary conditions are shown in Tables 1 and 2, respectively. The simulation parameters correspond to a lab-scale spray fluidized bed coating process in which glass beads are coated with a sodium benzoate solution. The specific heat capacity of glass particles is taken from Kuchling,[47] the coefficient of restitution is taken from Terrazas-Velarde et al[34] and the height of surface asperities (surface roughness) is assumed to be small, in the range of 1 μm, following Dernedde.[48] The collision velocity is calculated according to a method presented by Dernedde,[48] which yields distributions of collision velocity based on particle imaging velocimetry measurements in a pseudo-2D fluidized

TABLE 1 Simulation parameters (parameters for the reference case are printed in bold)

Parameter	Value	Unit
Bed diameter x_{bed}	0.15	m
Spraying rate $\dot{M}_{spray}$	0.7	kg h^{-1}
Mass flow rate of the fluidization gas $\dot{M}_g$	40	kg h^{-1}
Mass-transfer coefficient β	0.012, **0.013**, 0.014	m s^{-1}
Particle density ϱ_p	2,500	kg m^{-3}
Solid density ϱ_s	1,440	kg m^{-3}
Coefficient of restitution e	0.8	–
Height of surface asperities h_a	1	μm
Droplet diameter x_{drop}	25, **50**, 100	μm
Contact angle θ	20, **40**, 60	°
Collision velocity v_{coll}	0.42	m s^{-1}
Solid mass fraction w_s	30	%
Specific heat capacity of particles c_p	729	J kg^{-1} K^{-1}
Solid layer porosity ε	30	%

TABLE 2 Initial and boundary conditions (parameters for the reference case are printed in bold)

Parameter	Value	Unit
$Gn(t, x = 0)$	0	s^{-1}
$n(t = 0, x)$	$n_0 = f(x_0, \sigma_0)$	mm^{-1}
x_0	0.2	mm
σ_0	0.05	mm
$\Psi(t = 0)$	0	–
$Y_{in} = Y(t, \zeta = 0) = Y(t = 0, \zeta)$	1	g kg^{-1}
$T_{g,in} = T_g(t, \zeta = 0) = T_g(t = 0, \zeta)$	50, **70**, 95	°C
$X(t = 0)$	0	g kg^{-1}
$T_l(t = 0)$	20	°C
$M_p(t = 0)$	0.5	kg
$T_p(t = 0)$	50, **70**, 95	°C

bed. In the current study, the mean collision velocity is used in the model. Note that at this stage the calculated collision velocity is kept constant (i.e., it is not adjusted according to changing particle properties during the simulation). A more detailed description of this method is also given by Rieck et al[49] in the frame of Monte Carlo modeling. Note that the values given for the mass-transfer coefficient in Table 1 correspond to the initial values since β decreases over time due to size enlargement. The viscosity of the sodium benzoate solution has been measured using a Höppler viscometer at temperatures between 15 and 50°C. The viscosity is relatively low (i.e., 4.18 mPa s at a temperature of 20°C). Following Poling et al,[50] who suggest an exponential function to describe the influence of temperature on viscosity, an empirical correlation was obtained based on the experimental data:

$$\ln\eta = A + \frac{B}{T + 273.15}. \tag{47}$$

In this equation, T is the temperature (in °C) and A and B are constants. For the considered solution (aqueous sodium benzoate solution with a solid mass fraction of 30%) $A = -7.31$ and $B = 2{,}545$ K. Note that with these constants the viscosity is obtained in mPa s. In the model, the viscosity is calculated as a function of liquid film temperature T_l using Equation (47). In the simulations denoted by "low viscosity" values calculated with Equation (47) are used. In simulations denoted by "high viscosity," the viscosity is calculated with the same equation, but multiplied with a factor of 3 mimicking an increased viscosity due to the addition of thickener. The resulting viscosity at 20°C is then 12.54 mPa s. Depending on the material, even higher viscosity values are possible, see Dewettinck et al,[9] who used different gums as coating material. In the following section, results of the study are presented.

3 | RESULTS

In Figure 6, the probability of successful wet collisions calculated according to Equation (13) is compared to results obtained with the above described Monte Carlo model. In this example, the same particle-size distribution as in Figure 2 was used and the critical diameter was varied between 0.15 and 0.4 mm. An increasing critical diameter leads to larger values for $P_{\text{coll, wet, suc}}$ since the fraction of particles with fulfilled Stokes criterion is increased. The results obtained with both models agree well.

Figure 7 shows the transient behavior of the particle-size distribution and the influence of the inlet gas temperature on the wet surface fraction, viscosity, and the critical diameter during 1 h of process time. Figure 7a shows the transient behavior of the particle-size distribution due to layering growth. The shape of the distribution is preserved, while its mean value increases from 0.2 to 0.26 mm. Figure 7b shows the wet surface fraction for different temperatures. An increasing inlet gas temperature leads to a higher evaporation capacity of the gas and therefore to a larger evaporation rate. As a result, the wet surface fraction decreases from 0.29 (50°C) to 0.01 (95°C). The viscosity of the solution decreases if the inlet gas temperature is increased, due to a correspondingly higher liquid film temperature, see Figure 7c. The critical diameter decreases with increasing inlet gas temperature as well, see Figure 7d. Therefore, particles are more likely to form agglomerates at low temperatures due to the combination of higher wet surface fraction (probability of wet collisions) and higher critical diameter (probability of successful wet collisions).

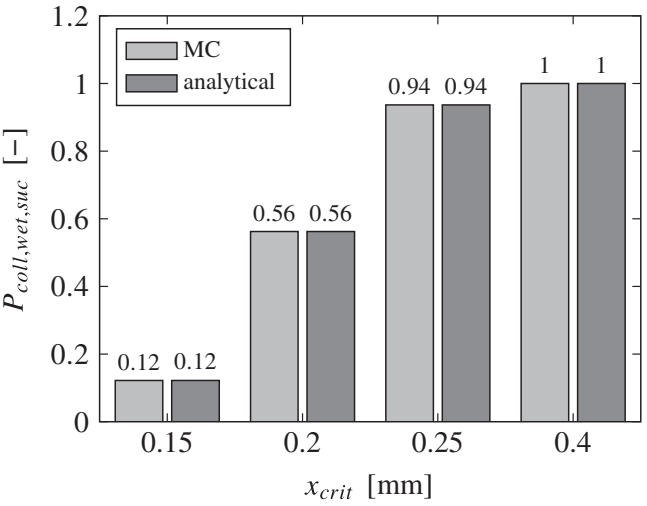

FIGURE 6 Comparison of the probability of successful wet collisions obtained with the proposed analytical model and a Monte Carlo model

The mentioned probabilities are given in Figure 8. The probability of wet collisions is shown in Figure 8a, following the behavior of the wet surface fraction, see Figure 7b. The probability of wet collisions ranges between 0.5 (50°C) and 0.02 (95°C). Figure 8b and Figure 8c show the probability of successful wet collisions both for low and high viscosities. The temperature dependency is the same in both cases: an increasing inlet gas temperature leads to smaller values since the critical diameter is decreased, see Figure 7d. In case of low viscosity, the values are very small, indicating that wet collisions are rarely successful. However, if the viscosity is increased, the probability of successful wet collisions is significantly increased. The values then range between 0.3 (50°C) and 0.0005 (95°C). Figure 8d,e shows the probability of successful collisions, which is the product of the probability of wet collisions (shown in Figure 8a) and the probability of successful wet collisions (shown in Figure 8b,c). Agglomeration seems unlikely in case of low viscosity since the resulting values are smaller than 0.001 for all temperatures. In case of high viscosity, agglomeration may occur at an inlet gas temperature of 50°C since up to 15% of all collisions are successful. For higher temperatures, the values of $P_{\text{coll,suc}}$ are smaller than 0.001 indicating that agglomeration is unlikely. The influence of temperature and viscosity on the considered probabilities is summarized in Table 3.

The influence of the wetting parameters (droplet size and contact angle) on the wet surface fraction and the corresponding probability of wet collisions is shown in Figure 9 and Table 3. Since the simulation results in Figure 8 indicate that agglomeration is unlikely above an

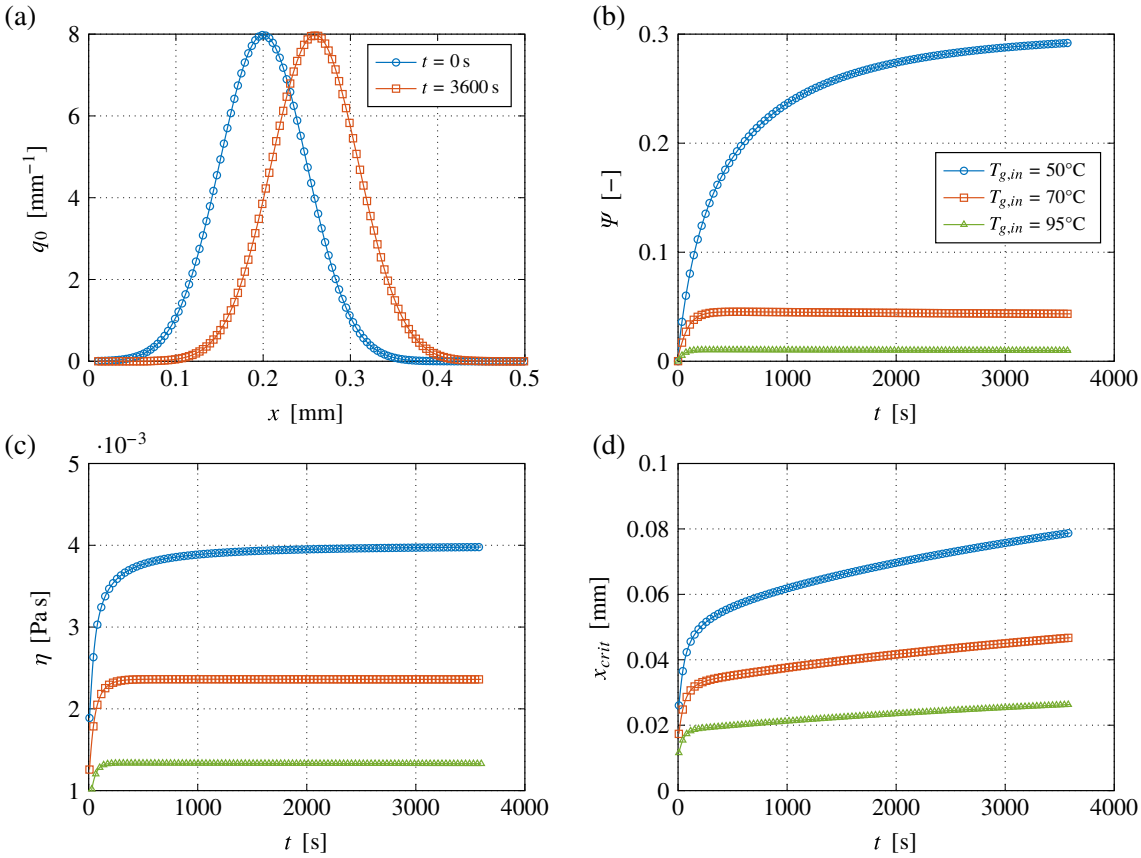

FIGURE 7 Plot of the particle-size distribution (before and after layering growth) (a), and influence of the inlet gas temperature on the wet surface fraction (b), liquid viscosity (c), and the critical particle diameter (d) [Color figure can be viewed at wileyonlinelibrary.com]

inlet gas temperature of 50°C for the chosen simulation parameters, only results for 50°C are given in Figure 9. Figure 9a shows that smaller droplets and contact angles lead to an increased wet surface fraction. A smaller droplet size leads to a decreased contact area $A_{contact}$ and droplet mass M_{drop}. Since $A_{contact}\tilde{x^2_{drop}}$ and $M_{drop}\tilde{x^3_{drop}}$, the wet surface fraction increases for smaller droplets (cf. Equation 17). At the same time, the evaporation rate (cf. Equation 31) is increased since the wet surface fraction is higher, while the ratio between the curved surface area A_{drop} and the contact area $A_{contact}$ is constant. As a result, the mass of the liquid film phase is smaller, which would in turn decrease the wet surface fraction. Eventually, the first effect prevails and the wet surface fraction increases for smaller droplet sizes. A smaller contact angle increases the contact area $A_{contact}$, while the droplet mass stays constant, leading to a larger wet surface fraction (cf. Equation 17). Therefore, the evaporation rate is increased as well. At the same time, the ratio between the curved surface area A_{drop} and the contact area $A_{contact}$ is reduced, which would decrease the evaporation rate (cf. Equation 31). In this case, the influence of the wet surface fraction prevails and the evaporation rate is increased. Similar to the above discussed influence of the droplet size, this would lead to a smaller mass of the liquid film phase and a smaller wet surface fraction. Eventually, the influence of the contact angle on the wet surface fraction through Equation 17 is predominant and the wet surface fraction increases if the contact angle is smaller. Figure 9b shows the behavior of the corresponding probability of wet collisions following the trend of the wet surface fraction.

Figure 10 and Table 3 show the influence of the wetting parameters (droplet size and contact angle) on the probability of successful wet collisions and the probability of successful collisions for low and high viscosity at an inlet gas temperature of 50°C. The probability of successful wet collisions decreases for smaller droplet sizes and contact angles, see Figure 10a,b. In both cases the droplet height is decreased (cf. Equation 20) leading to smaller critical diameters (cf. Equation 5) and correspondingly smaller values of $P_{coll,wet,suc}$. In case of a low viscosity the probability of successful wet collisions is small, while in case of a high viscosity $P_{coll,wet,suc}$ is significantly increased. Figure 10c,d shows the probability of successful collisions obtained by multiplying the probability of wet collisions (see Figure 9(b)) and the probability of successful wet collisions (see Figure 10a,b). Although the values of the probability of wet collisions are relatively high, ranging between 0.4 and 0.6, the probability of successful collisions is low when a low viscosity is used due to a small probability of successful wet collisions. Agglomeration is unlikely since $P_{coll,suc}$ is smaller than 0.001 in all cases. For a high viscosity, the probability of successful collisions is significantly larger due to the increased probability of successful wet collisions. Significant agglomeration is to be expected since $P_{coll,suc}$ is larger than 0.001 in all simulations,

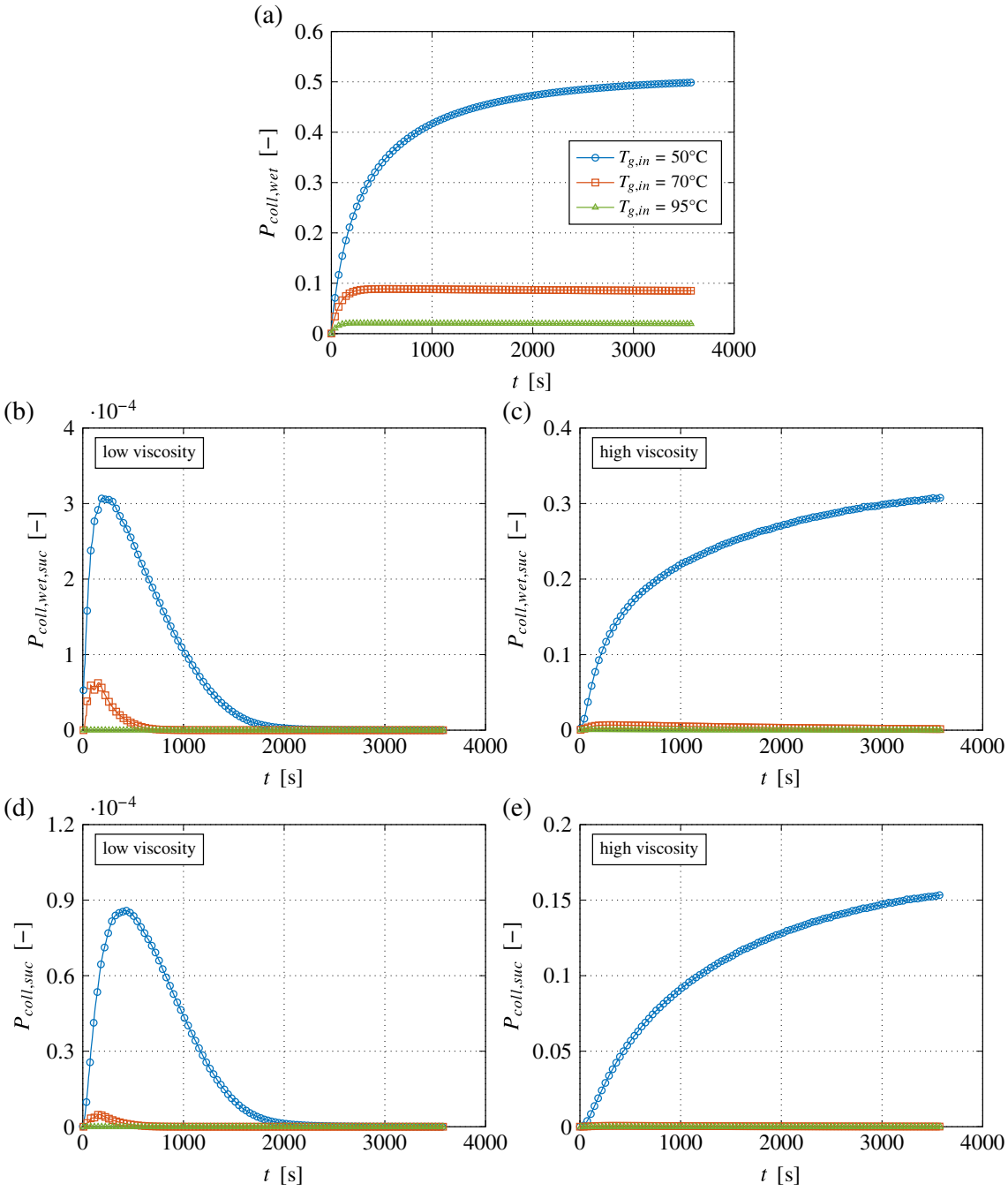

FIGURE 8 Influence of the inlet gas temperature on the probability of wet collisions (a), the probability of successful wet collisions for a low viscosity (b) and a high viscosity (c), and the probability of successful collisions for a low viscosity (d) and a high viscosity (e) [Color figure can be viewed at wileyonlinelibrary.com]

TABLE 3 Summarized influence of the inlet gas temperature, droplet size, contact angle, and liquid viscosity on the probability of wet collisions, probability of successful wet collisions, and the probability of successful collisions

	$T_{g,\,in}$ ↑	x_{drop} ↑	θ ↑	η ↑
$P_{coll,\,wet}$	↓	↓	↓	–
$P_{coll,\,wet,\,suc}$	↓	↑	↑	↑
$P_{coll,suc}$	↓	↑	↑	↑

especially for large droplet sizes and contact angles since up to 35% of all collisions are successful.

The above shown simulation results show that the inlet gas temperature, liquid viscosity and the wetting parameters impact the probability of successful collisions and therefore the dominant size enlargement mechanism. In order to link the probability of successful collisions with the dominant size enlargement mechanism, classification based on simulations and experimental data is presented in the following.

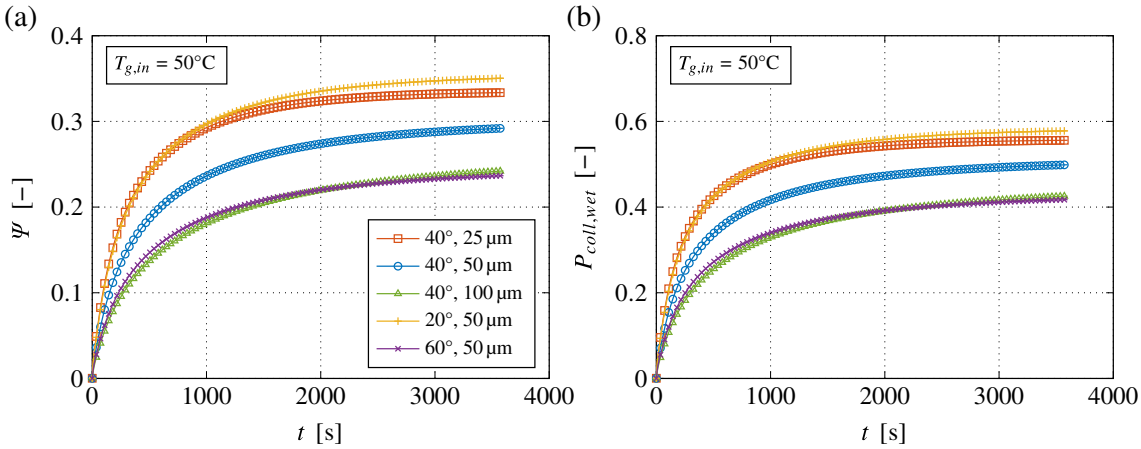

FIGURE 9 Influence of droplet size and contact angle on the wet surface fraction (a) and the probability of wet collisions (b) [Color figure can be viewed at wileyonlinelibrary.com]

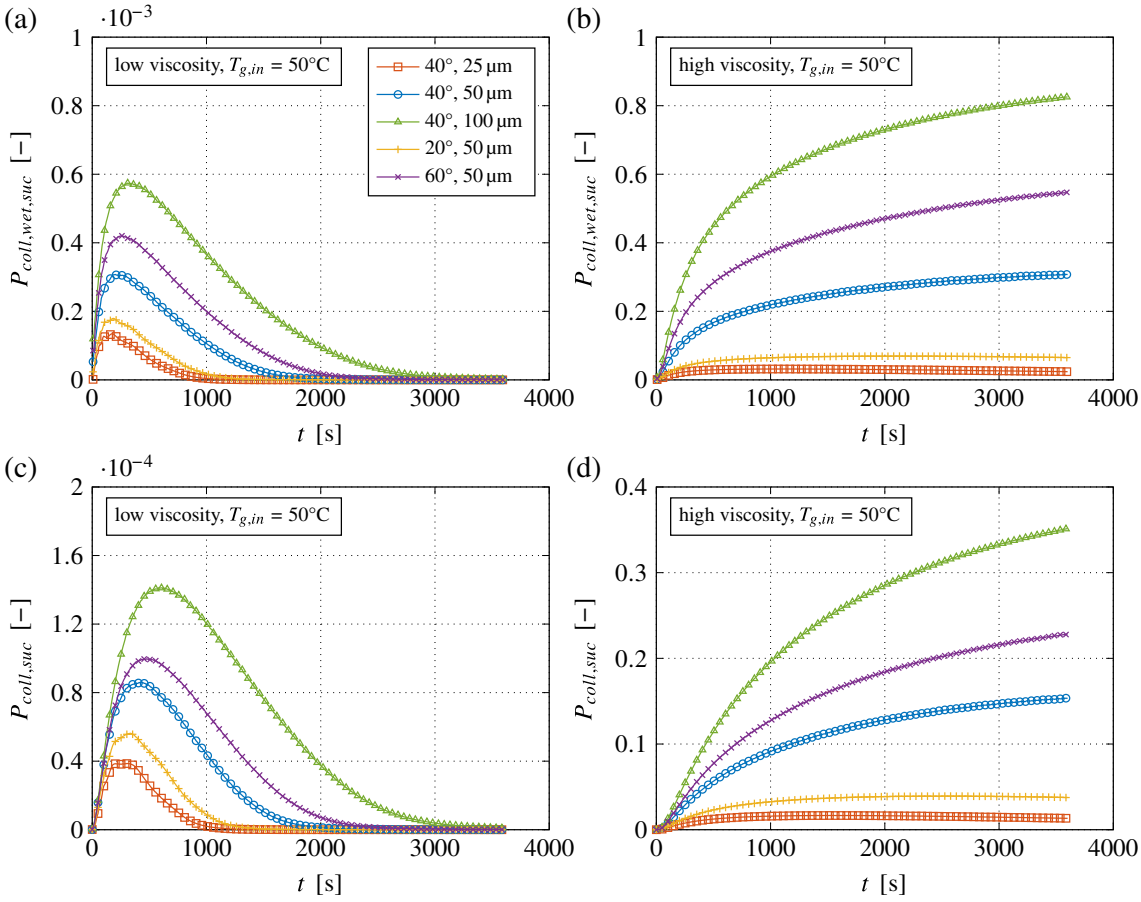

FIGURE 10 Influence of droplet size and contact angle on the probability of successful wet collisions for a low viscosity (a) and a high viscosity (b), and the probability of successful collisions for a low viscosity (c) and a high viscosity (d) [Color figure can be viewed at wileyonlinelibrary.com]

3.1 | Classification of the dominant size enlargement mechanism

In order to classify the dominant size enlargement mechanism based on the probability of successful collisions, several simulations have been performed corresponding to experimental investigations of spray fluidized bed processes available in the literature. In these studies, one size enlargement mechanism is dominant, which is in each case determined by the author of the respective study (e.g., by SEM images, or measuring either the particle-size distribution or the

fraction of agglomerated particles). In the simulation, the dominant size enlargement mechanism is principally unknown. Therefore, particle growth is not considered in these simulations (i.e., the initial particle-size distribution and particle density are kept constant). The simulations are performed until the considered probabilities reach a steady state. These values are used to characterize the conditions in each simulation, which are then linked to the dominant size enlargement mechanism determined by the author of the study. Comments on the selection of the simulation parameters of each study are given below before presenting the results.

In this work, three studies focusing on spray fluidized bed agglomeration performed by Hampel,[51] Terrazas-Velarde,[52] Jiménez et al[53] and three studies dealing with layering growth performed by Rieck et al[27] and Saleh et al[54,55] are considered. For each study, several simulations were performed according to the experimental parameters. The corresponding simulation parameters are shown in Table 4. Hampel[51] and Terrazas-Velarde[52] both used non-porous glass beads and porous γ-Al_2O_3 particles, which were agglomerated using an aqueous HPMC (hydroxypropyl-methylcellulose) solution. Jiménez et al[53] also used glass beads, which were agglomerated using an aqueous solution of acacia gum. The experiments were performed in a conical fluidized bed with a diameter of 140 mm at the bottom and 225 mm at the top. Since the presented model is derived for cylindrical fluidized bed chambers, a mean diameter of the chamber is used in the simulation to obtain a similar flow regime (bed porosity). Jiménez et al[53] report a relatively high bed porosity larger than 0.95, which is also achieved in the simulation using a mean diameter of the fluidized bed chamber. Rieck et al[27] deal with spray fluidized bed coating of glass beads and γ-Al_2O_3 particles using a sodium benzoate solution. Saleh et al[54,55] focus on coating of sand particles by spraying a sodium chloride solution. In both studies, the mass flow rate of the fluidization gas was not directly given. Instead, the excess gas velocity was reported, which was used to calculate the corresponding mass flow rate with the given diameter of the fluidized bed chamber. Additionally, the bed temperature was given instead of the inlet gas temperature. Therefore, we adjusted the inlet gas temperature in the simulation to fit the bed temperature given by Saleh et al.[54,55] The moisture content of the inlet gas depends on how the fluidization gas flow is generated. In case of Rieck et al,[27] Hampel,[51] Terrazas-Velarde,[52] and Saleh et al[54,55] pressurized air, which is usually dry, is used. In these cases, 1 g kg^{-1} is assumed. Jiménez et al[53] do not explain the generation of the gas flow, but according to Jiménez[56] a fan is used for fluidization by means of ambient air. In this case, we assume a value of 9 g kg^{-1} based on 20°C and a relative humidity of 60%.

In each study, most of the necessary material parameters were given along with the process parameters. However, some other parameters were missing and had to be either assumed or taken from other sources. References and estimation methods regarding the material parameters are summarized below.

- The particle densities were in any case given by the authors in the respective study.
- The coefficient of restitution of glass beads and γ-Al_2O_3 particles are given by Terrazas-Velarde[52] based on literature values. The restitution coefficient of sand particles is taken from Derakhshani et al.[57]
- Contact angles between aqueous HPMC and glass beads or γ-Al_2O_3 particles are given by Terrazas-Velarde[52] based on photo-optical measurements. Values for the other systems (acacia gum-glass, sodium benzoate-glass, sodium benzoate-γ-Al_2O_3, sodium chloride-sand) were not available in the literature. The measurements performed by Terrazas-Velarde[52] show that the influence of the solid mass fraction on the contact angle is negligible. Based on this observation and since all liquids used in the considered experimental studies are water-based, we estimate the contact angle for the systems acacia gum-glass, sodium benzoate-glass, and sodium chloride-sand to be 40° and 60° in case of sodium benzoate-γ-Al_2O_3.
- The droplet sizes were given by the original authors in case of Hampel,[51] Terrazas-Velarde,[52] and Saleh et al.[54,55] Jiménez et al[53] report some values, but do not present detailed information. For a reference experiment 35 μm are given, which is used in each of the corresponding simulations. In case of Rieck et al[27] the droplet size was not given, but they were subsequently calculated using an empirical correlation for externally mixing two-fluid nozzles reported by Lefebvre and McDonell.[58] Therefore, the surface tension of the sodium benzoate solution was measured at 20°C (using a Du Noüy tensiometer) resulting in 60.74 mN m^{-1}. The corresponding droplet diameters are in the range of 60 μm, which is the value used in the simulations.
- The height of surface asperities for glass and γ-Al_2O_3 particles are taken from Dernedde.[48] In case of sand particles no values were available. Therefore it is assumed that the surface structure of sand and glass particles is similar and thus the same value is used.
- The specific heat capacity of the particles is taken from literature: Kuchling[47] (glass and sand), and Burgschweiger et al[37] (γ-Al_2O_3).
- The viscosity of aqueous HPMC was taken from Dernedde[48] and the viscosity of aqueous sodium chloride was taken from Zhang and Han.[59] The viscosity of the acacia gum solution was directly given by Jiménez et al.[53] Since the temperature dependency of the above mentioned viscosities is unknown, constant values were used. In case of Rieck et al,[27] the above mentioned correlation based on measured viscosities (see Equation 47) was used.
- The density of the sprayed solid was directly given by Hampel,[51] Terrazas-Velarde,[52] and Rieck et al[27] in case of HPMC and sodium benzoate, respectively. The values for acacia gum and sodium chloride are taken from safety data sheets.[60,61]
- The measured particle-size distributions were available in case of Rieck et al,[27] Hampel,[51] Saleh et al[54] in the form of either files or tables. In case of Terrazas-Velarde,[52] plots of the measured particle-size distributions of the glass beads and γ-Al_2O_3 particles were given. Normal distributions were then created in the simulation to visually fit the plots of the distributions. In case of Jiménez et al,[53] Saleh et al[55] no plots or data were available other than the mean diameter. In these cases a normal distribution was used as

TABLE 4 Simulation parameters for each experimental study used to derive the classification of the dominant size enlargement mechanism

Parameter	Hampel[51]	Terrazas-Velarde[52]	Jiménez et al[53]	Rieck et al[27]	Saleh et al[54]	Saleh et al[55]	Unit
Particle material	Alumina (A) Glass (G)	Alumina (A) Glass (G)	Glass	Alumina (A) Glass (G)	Sand	Sand	
Sprayed solid material	HPMC	HPMC	Acacia gum	NaB	NaCl	NaCl	
Sprayed liquid material	Water	Water	Water	Water	Water	Water	
Dominant mechanism	Agglomeration	Agglomeration	Agglomeration	Layering	Layering	Layering	
Bed diameter x_{bed}	0.15	0.15	0.184	0.15	0.1	0.1	m
Bed mass M_p	0.5 (A)	0.3 (A)	0.25–0.75	0.5 (A)	1.25–2.53	2	kg
	0.85 (G)	0.5 (G)		1 (G)			
Spraying rate $\dot{M}_{spray}$	0.2–0.3	0.1–0.5	0.172–0.502	0.5–1.28	0.274–0.598	0.46	kg h^{-1}
Mass flow rate of the fluidization gas $\dot{M}_g$	20–30	58 (A)	160	75 (A)	11	10–17.5	kg h^{-1}
		70–110 (G)		120 (G)			
Inlet temperature of the fluidization gas $T_{g,\,in}$	50–100	30–80	60–80	50–95	185–255	100–145	°C
Inlet moisture content of the fluidization gas Y_{in}	1	1	9	1	1	1	g kg^{-1}
Mass-transfer coefficient β	0.002–0.004 (A)	0.020 (A)	0.023–0.054	0.023–0.026 (A)	0.002–0.003	0.002–0.005	m s^{-1}
	0.003–0.004 (G)	0.027–0.038 (G)		0.032–0.037 (G)			
Particle density ϱ_p	1,040 (A)	1,400 (A)	2,450	1,280 (A)	2,630	2,630	kg m^{-3}
	2,500 (G)	2,500 (G)		2,500 (G)			
Solid density ϱ_s	1,390	1,390	1,400	1,440	2,170	2,170	kg m^{-3}
Coefficient of restitution e	0.6 (A)	0.6 (A)	0.8	0.6 (A)	0.9	0.9	–
	0.8 (G)	0.8 (G)		0.8 (G)			
Height of asperities h_a	5 (A)	5 (A)	1	5 (A)	1	1	μm
	1 (G)	1 (G)		1 (G)			
Droplet diameter x_{drop}	40	80	35	60	15–60	20	μm
Contact angle θ	60 (A)	60 (A)	40	60 (A)	40	40	°
	40 (G)	40 (G)		40 (G)			
Collision velocity v_{coll}	0.16–0.24 (A)	1.17 (A)	0.88	2.16 (A)	0.23	0.28–1.20	m s^{-1}
	0.13–0.19 (G)	1.53–2.26 (G)		2.82 (G)			
Solution viscosity η	5.98 (2%)	21.44 (4%)	43 (20%) 200 (30%)	4.18 (20°C; Equation (47) used)	1.05 (10%)	1.26	mPas
	21.44 (4%)	147.11 (8%)			1.26 (20%)		
	61.86 (6%)	383.90 (10%)			1.40 (25%)		
Solid mass fraction w_s	2–6	4–10	20–30	30	10–25	20	%
Specific heat capacity particles c_p	944 (A)	944 (A)	729	944 (A)	840	840	J kg^{-1} K^{-1}
	729 (G)	729 (G)		729 (G)			
Particle diameter x	150 (A)	360 (A)	160	610 (A)	229	267–639	μm
	120 (G)	400 (G)		530 (G)			
Number of simulations	22	14	8	8	8	3	–

Abbreviation: HPMC, hydroxypropyl-methylcellulose.

well, where the standard deviation was set to 10% of the mean diameter.

- The collision velocity was calculated for each simulation using the method proposed by Dernedde[48] as described above. In a study presented by Rieck et al,[49] the collision velocities calculated with this method were in the same range as values which had experimentally been obtained by Jiang et al[62] using particle tracking velocimetry.

The results are shown in Figure 11. The coordinate axes represent the probability of wet collisions and the probability of successful wet collisions, respectively. Contour lines indicate the level of the probability of successful collisions. As described above, for each simulation the steady-state values of the mentioned probabilities are calculated. This allows to draw one data point for each simulation into the plot. It can be seen that the simulations corresponding to the experiments in which layering is dominant are located on the left side of the plot, where the probability of successful wet collisions is low. In fact, the values in these simulations equal 0 in any case, while the steady-state probability of wet collisions ranges between 0.00016 and 0.3. The simulations corresponding to the experiments in which agglomeration is dominant, are located on the right side of the plot at a high probability of successful wet collisions. These values range between 0.92 (one point) and 1, while the probability of wet collisions ranges between 0.0014 and 0.42. Exceptions are three data points which belong to agglomeration experiments performed by Terrazas-Velarde.[52] These are placed on the left side of the plot due to low probability of successful wet collisions predicted by the simulation. In the corresponding experiments, the lowest amount of HPMC (4%) was used, which leads to a relatively low viscosity. Terrazas-Velarde[52] reports, that during experiments using a solid mass fraction of 4% an initial nongrowth period was observed due to nonfulfilled Stokes criterion. Therefore, agglomeration should not be possible, which would agree with the findings in this work. However, during drying of the droplets, a significant increase in viscosity is observed (up to values in the range of 10 Pa s), eventually leading to a fulfilled Stokes criterion and therefore agglomeration. Since at this stage the initial liquid properties are used and changing liquid properties during drying are not taken into account, the presented model cannot predict the dominant size enlargement mechanism for these experiments. Nevertheless, the data shown in Figure 11 allows to classify the dominant size enlargement mechanism based on the probability of successful collisions. The simulation study indicates that the border between layering and agglomeration can be characterized by $P_{coll,suc}$ = 0.001. This means that for agglomeration to become dominant, the probability of successful collisions does not need to be high (i.e., in the range of 0.5 or higher). Instead, exceeding a rather small value of 0.001 is enough to shift the dominant size enlargement mechanism toward agglomeration. Consequently, layering will be dominant when the probability of successful collisions is lower than 0.001. Based on this classification, the agglomeration regime and the layering regime are represented by the gray and white areas in Figure 11, respectively. Additionally, a sensitivity analysis to the collision velocity has been performed. All simulations shown in Figure 11 were repeated twice with a small collision velocity (reduced by 50% compared to the original value) and a high collision velocity (increased by 50% compared to the original value). Although the collision velocity was varied in this relatively wide range, the border between layering and agglomeration may still be described by $P_{coll,suc}$ = 0.001 in both cases.

3.2 | Regime maps

Based on the classification shown above, it is also possible to create regime maps showing the influence of actual process parameters rather than probabilities on the dominant size enlargement mechanism. In this study, two regime maps, each based on 3,000 simulations, were created using the same parameters as in the previously shown simulation study, see Tables 1 and 2. The parameters of the reference case are used here, while the inlet gas temperature is varied between 40 and 100°C (Figure 12a) and the spraying rate is varied between 0 kg h^{-1} and 1.2 kg h^{-1} (Figure 12b). The viscosity is varied as well using a constant factor between 1 and 10. The contour lines in Figure 12 represent the different levels of the probability of successful collisions. Gray and white areas illustrate the agglomeration and layering regimes. The results show, as expected, that agglomeration becomes dominant for low temperatures and high viscosities as well as high spraying rates and high viscosities.

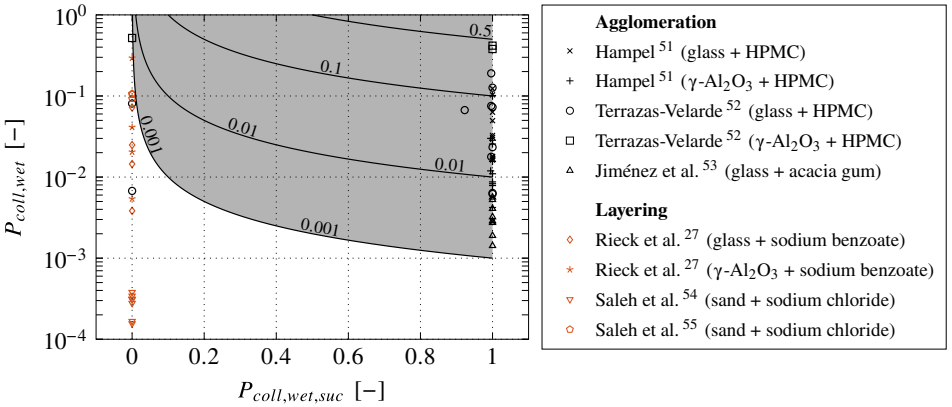

FIGURE 11 Regime map consisting of contour lines illustrating different levels of the probability of successful collisions and data points representing simulation results corresponding to experimental investigations available in the literature [Color figure can be viewed at wileyonlinelibrary.com]

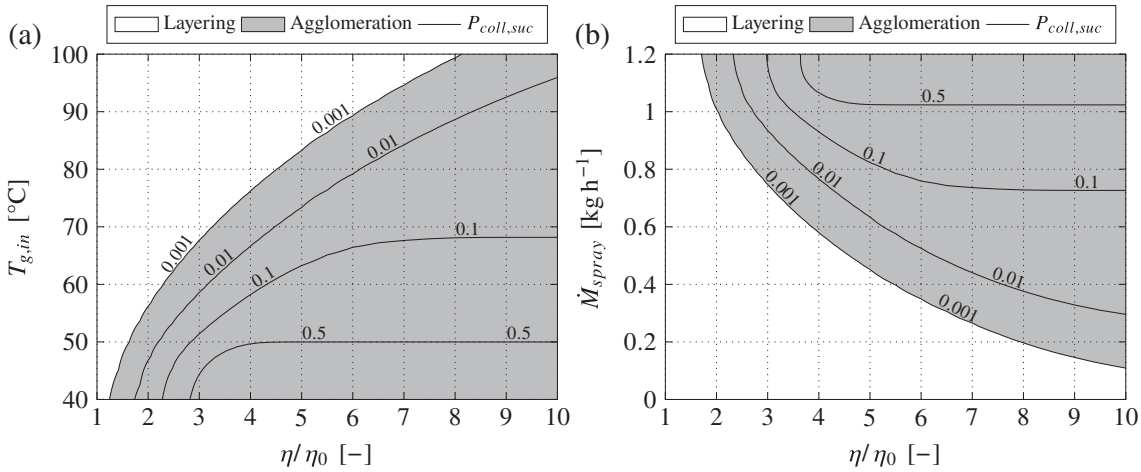

FIGURE 12 Regime maps obtained for the simulation parameters given in Tables 1 and 2 for a changing inlet gas temperature (a) and spraying rate (b)

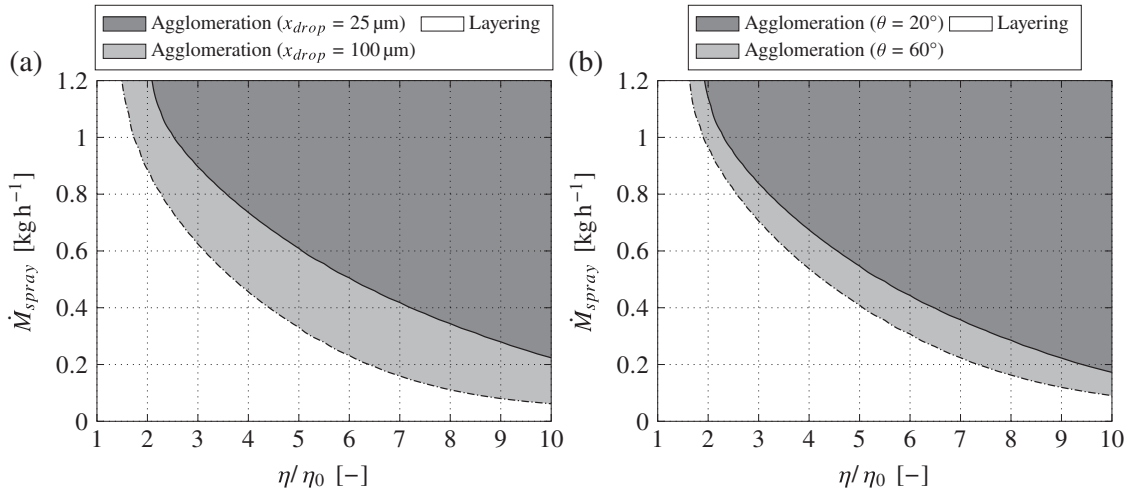

FIGURE 13 Influence of droplet size (a) and contact angle (b) on the size of the agglomeration and layering regime

The influence of the wetting parameters can also be shown using regime maps. Figure 13 shows the border between the size enlargement mechanisms (defined by $P_{coll,suc}$ = 0.001) for different droplet sizes and contact angles. The simulation parameters are identical to the ones shown in Tables 1 and 2. The regime map is drawn for two droplet sizes (25 and 100 µm) and contact angles (20° and 60°). As discussed above, large droplet sizes and contact angles favor agglomeration, which can be seen in Figure 13 as well since the area representing dominant agglomeration is larger in these cases.

4 | CONCLUSION AND OUTLOOK

The presented work deals with estimating the dominant size enlargement mechanism in spray fluidized bed processes. Therefore, a process model for spray fluidized bed layering based on population balances and a heat- and mass-transfer model was developed. New methods to calculate the wet surface fraction based on the droplet geometry and to incorporate the Stokes criterion into the model are presented, allowing the calculation of the probability of wet collisions and the probability of successful wet collisions, respectively. As a result, the probability of successful collisions can be obtained, which may then be used to estimate the dominant size enlargement mechanism occurring as a result of process and material parameters. A simulation study was performed to investigate the influence of the inlet gas temperature and wetting parameters (droplet size and contact angle) on the mentioned probabilities. The study shows that the probability of wet collisions decreases for higher inlet gas temperatures and larger droplet sizes and contact angles, while the probability of successful wet collisions decreases for higher inlet gas temperatures as well, but increases for larger droplet sizes and contact angles. In total, the probability of successful collisions, and therefore the agglomeration tendency, decreases when the inlet gas temperature is high and increases for large droplet sizes and contact angles. Simulations based on experimental work published in the

literature were performed enabling a classification of the dominant size enlargement mechanism based on the calculated probability of successful collisions. The results indicate that exceeding a probability of successful collisions of 0.001 is sufficient for agglomeration to become dominant. Consequently, layering will be dominant when the probability of successful collisions is smaller than 0.001. The proposed classification allows for the creation of regime maps, which clearly present the influence of process and material parameters on the border between the two size enlargement mechanisms. The presented model may be used without the population balance model (without growth, constant particle distribution) to estimate the dominant size enlargement mechanism occurring when a liquid is sprayed on a particle bed with certain process and material parameters. If the population balance model is taken into account (with growth, transient particle distribution), the dominant size enlargement mechanism can be estimated during a layering process.

Future work should focus on extending the model by taking into account changing droplet properties (i.e., geometry and viscosity) during drying. It was shown that considering only the initial droplet properties may lead to predicting the wrong size enlargement mechanism if the droplet properties change strongly. This can be implemented using another population balance to consider the residence time distribution of droplets. Then, changes in droplet properties can be calculated from the residence time of the droplet. The population balance model should be extended to account for simultaneous layering and agglomeration by incorporating the probability of successful collisions into the aggregation kernel. Further extensions may be implemented to improve the predictive ability of the model such as taking into account different zones in the fluidized bed chamber (e.g., spraying and drying zones), droplet size distributions, and imbibition of liquid droplets into porous particles.

ACKNOWLEDGMENTS

We gratefully acknowledge the financial support of the Deutsche Forschungsgemeinschaft (DFG, German Research Foundation) within the priority program SPP 1679 (project A2). Partially funded by DFG—Project-ID 61375930—SFB/CRC 814 Additive Manufacturing.

ORCID

Christian Rieck https://orcid.org/0000-0003-4419-2633

REFERENCES

1. Turton R, Tardos GI, Ennis BJ. Fluidized bed coating and granulation. In: Yang WC, ed. *Fluidization, solids handling, and processing*. Westwood: Noyes Publications; 1999:331-434.
2. Pfalzer L, Bartusch W, Heiss R. Untersuchungen über die physikalischen Eigenschaften agglomerierter Pulver. *Chem Ing Tech*. 1973;45(8):510-516. https://doi.org/10.1002/cite.330450810.
3. Palzer S. Agglomeration of pharmaceutical, detergent, chemical and food powders: similarities and differences of materials and processes. *Powder Technol*. 2011;206(1–2):2-17. https://doi.org/10.1016/j.powtec.2010.05.006.
4. Westermarck S, Juppo AM, Kervinen L, Yliruusi J. Pore structure and surface area of mannitol powder, granules and tablets determined with mercury porosimetry and nitrogen adsorption. *Eur J Pharm Biopharm*. 1998;46(1):61-68. https://doi.org/10.1016/S0939-6411(97)00169-0.
5. Guignon B, Duquenoy A, Dumoulin ED. Fluid bed encapsulation of particles: principles and practice. *Drying Technol*. 2002;20(2):419-447. https://doi.org/10.1081/DRT-120002550.
6. Werner SRL, Jones JR, Paterson AHJ, Archer RH, Pearce DL. Air-suspension particle coating in the food industry: part I—state of the art. *Powder Technol*. 2007;171(1):25-33. https://doi.org/10.1016/j.powtec.2006.08.014.
7. Bück A, Tsotsas E, Sommer K. Size enlargement. *Ullmann's Encyclopedia of industrial chemistry*. Weinheim: Wiley-VCH Verlag GmbH & Co. KGaA; 2014:1-47.
8. Moraga SV, Villa MP, Bertín DE, et al. Fluidized-bed melt granulation: the effect of operating variables on process performance and granule properties. *Powder Technol*. 2015;286:654-667. https://doi.org/10.1016/j.powtec.2015.09.006.
9. Dewettinck K, Deroo L, Messens W, Huyghebaert A. Agglomeration tendency during top-spray fluidized bed coating with gums. *Food Sci Technol*. 1998;31(6):576-584. https://doi.org/10.1006/fstl.1998.0421.
10. Dewettinck K, Messens W, Deroo L, Huyghebaert A. Agglomeration tendency during top-spray fluidized bed coating with gelatin and starch hydrolysate. *Food Sci Technol*. 1999;32(2):102-106. https://doi.org/10.1006/fstl.1998.0507.
11. Hemati M, Cherif R, Saleh K, Pont V. Fluidized bed coating and granulation: influence of process-related variables and physicochemical properties on the growth kinetics. *Powder Technol*. 2003;130(1–3):18-34. https://doi.org/10.1016/S0032-5910(02)00221-8.
12. Hede PD, Bach P, Jensen AD. Top-spray fluid bed coating: scale-up in terms of relative droplet size and drying force. *Powder Technol*. 2008a;184(3):318-332. https://doi.org/10.1016/j.powtec.2007.09.009.
13. Hede PD, Bach P, Jensen AD. Validation of the flux number as scaling parameter for top-spray fluidised bed systems. *Chem Eng Sci*. 2008b;63(3):815-828. https://doi.org/10.1016/j.ces.2007.10.017.
14. Boerefijn R, Hounslow MJ. Studies of fluid bed granulation in an industrial R&D context. *Chem Eng Sci*. 2005;60(14):3879-3890. https://doi.org/10.1016/j.ces.2005.02.021.
15. Boerefijn R, Dontula PR, Kohlus R. Detergent granulation. In: Salman AD, Hounslow MJ, Seville JPK, eds. *Handbook of powder technology: granulation*. Amsterdam: Elsevier Science B.V; 2007:673-703. https://doi.org/10.1016/S0167-3785(07)80049-2.
16. Akkermans JHM, Edwards MF, Groot ATJ, Montanus CPM, van Pomeren RWJ, Yüregir KAR. Production of detergent granulates. International Patent WO9858046; 1998.
17. Wasserman MI, Ridyard MW, Capeci SW, Beimesch WE, Mort PR III. Process for coating detergent granules in a fluidized bed. International Patent WO0078912. 2000.
18. Ennis BJ, Tardos GI, Pfeffer R. A microlevel-based characterization of granulation phenomena. *Powder Technol*. 1991;65(1–3):257-272. https://doi.org/10.1016/0032-5910(91)80189-P.
19. Davis RH. Elastohydrodynamic collisions of particles. *Physico Chem Hydrodyn*. 1987;9(1–2):41-52.
20. Barnocky G, Davis RH. Elastohydrodynamic collision and rebound of spheres: experimental verification. *Phys Fluids*. 1988;31(6):1324-1329. https://doi.org/10.1063/1.866725.
21. Donahue CM, Davis RH, Kantak AA, Hrenya CM. Mechanisms for agglomeration and deagglomeration following oblique collisions of wet particles. *Phys Rev E*. 2012a;86:021303. https://doi.org/10.1103/PhysRevE.86.021303.
22. Donahue CM, Brewer WM, Davis RH, Hrenya CM. Agglomeration and de-agglomeration of rotating wet doublets. *J Fluid Mech*. 2012b;708:128-148. https://doi.org/10.1017/jfm.2012.297.
23. Villa MP, Bertín DE, Cotabarren IM, Piña J, Bucalá V. Fluidized-bed melt granulation: coating and agglomeration kinetics and growth regime prediction. *Powder Technol*. 2016;300:61-72. https://doi.org/10.1016/j.powtec.2016.06.006.
24. Heinrich S, Mörl L. Fluidized bed spray granulation: a new model for the description of particle wetting and of temperature and

concentration distribution. *Chem Eng Process*. 1999;38(4–6):635-663. https://doi.org/10.1016/S0255-2701(99)00065-3.
25. Vreman AW, van Lare CE, Hounslow MJ. A basic population balance model for fluid bed spray granulation. *Chem Eng Sci*. 2009;64(21):4389-4398. https://doi.org/10.1016/j.ces.2009.07.010.
26. Silva DO, Tamiozzo LM, Duarte CR, Murata VV, Barrozo MAS. Modeling of seed coating in a spouted bed. *Drying Technol*. 2011;29(3):286-294. https://doi.org/10.1080/07373937.2010.490892.
27. Rieck C, Hoffmann T, Bück A, Peglow M, Tsotsas E. Influence of drying conditions on layer porosity in fluidized bed spray granulation. *Powder Technol*. 2015;272:120-131. https://doi.org/10.1016/j.powtec.2014.11.019.
28. Hounslow MJ, Ryall RL, Marshall VR. A discretized population balance for nucleation, growth, and aggregation. *AIChE J*. 1988;34(11):1821-1832. https://doi.org/10.1002/aic.690341108.
29. Kumar J, Peglow M, Warnecke G, Heinrich S, Mörl L. Improved accuracy and convergence of discretized population balance for aggregation: the cell average technique. *Chem Eng Sci*. 2006;61(10):3327-3342. https://doi.org/10.1016/j.ces.2005.12.014.
30. Hussain M, Kumar J, Tsotsas E. A new framework for population balance modeling of spray fluidized bed agglomeration. *Particuology*. 2015;19:141-154. https://doi.org/10.1016/j.partic.2014.06.005.
31. Abberger T. Population balance modelling of granulation. In: Salman AD, Hounslow MJ, Seville JPK, eds. *Handbook of powder technology: granulation*. Amsterdam: Elsevier Science B.V; 2007:1109-1186. https://doi.org/10.1016/S0167-3785(07)80059-5.
32. Rajniak P, Stepanek F, Dhanasekharan K, Fan R, Mancinelli C, Chern RT. A combined experimental and computational study of wet granulation in a Wurster fluid bed granulator. *Powder Technol*. 2009;189(2):190-201. https://doi.org/10.1016/j.powtec.2008.04.027.
33. Tardos GI, Khan MI, Mort PR. Critical parameters and limiting conditions in binder granulation of fine powders. *Powder Technol*. 1997;94(3):245-258. https://doi.org/10.1016/S0032-5910(97)03321-4.
34. Terrazas-Velarde K, Peglow M, Tsotsas E. Investigation of the kinetics of fluidized bed spray agglomeration based on stochastic methods. *AIChE J*. 2011;57(11):3012-3026. https://doi.org/10.1002/aic.12506.
35. Braumann A, Kraft M, Wagner W. Numerical study of a stochastic particle algorithm solving a multidimensional population balance model for high shear granulation. *J Comput Phys*. 2010;229(20):7672-7691. https://doi.org/10.1016/j.jcp.2010.06.021.
36. Meric RA, Erbil HY. Evaporation of sessile drops on solid surfaces: pseudospherical cap geometry. *Langmuir*. 1998;14(7):1915-1920. https://doi.org/10.1021/la970147c.
37. Burgschweiger J, Groenewold H, Hirschmann C, Tsotsas E. From hygroscopic single particle to batch fluidized bed drying kinetics. *Can J Chem Eng*. 1999;77(2):333-341. https://doi.org/10.1002/cjce.5450770220.
38. Glück B. *Zustands- und Stoffwerte: Wasser, Dampf, Luft; Verbrennungsrechnung*. 2nd ed. Berlin: Verlag für Bauwesen; 1991.
39. Groenewold H, Tsotsas E. Predicting apparent Sherwood numbers for fluidized beds. *Drying Technol*. 1999;17(7–8):1557-1570. https://doi.org/10.1080/07373939908917635.
40. Martin H. Heat transfer in fluidized beds. In: VDI eV, ed. *VDI heat atlas*. Berlin: Springer-Verlag; 2010:1301-1309.
41. Sherony DF. A model of surface renewal with application to fluid bed coating of particles. *Chem Eng Sci*. 1981;36(5):845-848. https://doi.org/10.1016/0009-2509(81)85037-3.
42. Wnukowski P, Setterwall F. The coating of particles in a fluidized bed (residence time distribution in a system of two coupled perfect mixers). *Chem Eng Sci*. 1989;44(3):493-505. https://doi.org/10.1016/0009-2509(89)85027-4.
43. Maronga SJ, Wnukowski P. Modelling of the three-domain fluidized-bed particulate coating process. *Chem Eng Sci*. 1997;52(17):2915-2925. https://doi.org/10.1016/S0009-2509(97)00112-7.
44. Neugebauer C, Bück A, Palis S, Mielke L, Tsotsas E, Kienle A. Influence of thermal conditions on particle properties in fluidized bed layering granulation. *Processes*. 2018;6(12):235. https://doi.org/10.3390/pr6120235.
45. Mörl L, Heinrich S, Peglow M. Fluidized bed spray granulation. In: Salman AD, Hounslow MJ, Seville JPK, eds. *Handbook of powder technology: granulation*. Vol 11. Amsterdam: Elsevier Science B.V; 2007:21-188. https://doi.org/10.1016/S0167-3785(07)80037-6.
46. Koren B. A robust upwind discretization method for advection, diffusion and source terms. In: Vreugdenhil CB, Koren B, eds. *Numerical methods for advection-diffusion problems*. Braunschweig: Vieweg; 1993:117-138.
47. Kuchling H. *Taschenbuch der Physik*. 14th ed. Leipzig: Fachbuchverlag; 1994.
48. Dernedde M. Modellierung der Wirbelschicht-Sprühagglomeration unter Berücksichtigung der Partikelstrukturbildung [PhD thesis]. Otto von Guericke University Magdeburg; 2013.
49. Rieck C, Schmidt M, Bück A, Tsotsas E. Monte Carlo modeling of binder-less spray agglomeration in fluidized beds. *AIChE J*. 2018;64(10):3582-3594. https://doi.org/10.1002/aic.16349.
50. Poling BE, Prausnitz JM, O'Connell JP. *The properties of gases and liquids*. 5th ed. New York: McGraw-Hill; 2001.
51. Hampel R. Beitrag zur analyse von kinetischen Einflüssen auf die Wirbelschicht-Sprühagglomeration [PhD thesis]. Otto von Guericke University Magdeburg; 2010.
52. Terrazas-Velarde K. *Monte Carlo simulation of fluidized bed spray agglomeration*. Göttingen: Sierke Verlag; 2010.
53. Jiménez T, Turchiuli C, Dumoulin ED. Particles agglomeration in a conical fluidized bed in relation with air temperature profiles. *Chem Eng Sci*. 2006;61(18):5954-5961. https://doi.org/10.1016/j.ces.2006.05.007.
54. Saleh K, Cherif R, Hemati M. An experimental study of fluidized-bed coating: influence of operating conditions on growth rate and mechanism. *Adv Powder Technol*. 1999;10(3):255-277. https://doi.org/10.1163/156855299X00334.
55. Saleh K, Steinmetz D, Hemati M. Experimental study and modeling of fluidized bed coating and agglomeration. *Powder Technol*. 2003;130(1–3):116-123. https://doi.org/10.1016/S0032-5910(02)00254-1.
56. Jiménez T. Agglomération de particules par voie humide en lit fluidisé. [PhD thesis]. AgroParisTech; 2007.
57. Derakhshani SM, Schott DL, Lodewijks G. Micro-macro properties of quartz sand: experimental investigation and DEM simulation. *Powder Technol*. 2015;269:127-138. https://doi.org/10.1016/j.powtec.2014.08.072.
58. Lefebvre AH, McDonell VG. *Atomization and sprays*. 2nd ed. Boca Raton, FL: CRC Press; 2017.
59. Zhang HL, Han SJ. Viscosity and density of water + sodium chloride + potassium chloride solutions at 298.15 K. *J Chem Eng Data*. 1996;41(3):516-520. https://doi.org/10.1021/je9501402.
60. Carl Roth GmbH + Co KG. Safety data sheet according to 1907/2006/EC, article 31: Gum arabic, spray dried. 2014.
61. Carl Roth GmbH + Co KG. Voluntary safety information following the safety data sheet format according to regulation (EC) No. 1907/2006: Sodium chloride > 99,8%, with anticaking. 2018.
62. Jiang Z, Hagemeier T, Bück A, Tsotsas E. Experimental measurements of particle collision dynamics in a pseudo-2D gas-solid fluidized bed. *Chem Eng Sci*. 2017;167:297-316. https://doi.org/10.1016/j.ces.2017.04.024.

SUPPORTING INFORMATION

Additional supporting information may be found online in the Supporting Information section at the end of this article.

How to cite this article: Rieck C, Bück A, Tsotsas E. Estimation of the dominant size enlargement mechanism in spray fluidized bed processes. *AIChE J*. 2020;66:e16920. https://doi.org/10.1002/aic.16920